Pattern formation in Rayleigh-Bénard convection in a cylindrical container

Sten Rüdiger and Fred Feudel

Institut für Physik, Universität Potsdam, PF 601553, D-14415 Potsdam, Germany

We report on numerical investigations of pattern formation in the classical Rayleigh-Bénard convection with cylindrical geometry in the regime of low Prandtl numbers and moderate aspect ratio. Beyond the onset of convection, we found straight and bent rolls as stable patterns. By increasing the Rayleigh number, we studied the generation of defects, their dynamics in the form of climbing and gliding, the existence of stable targets and spirals as well as the occurrence of core instabilities, a variety of pattern types that were also observed in experiments.

I. INTRODUCTION

Convection in a fluid layer heated from below (Rayleigh-Bénard convection) provides many examples of complex pattern formation and constitutes a model for transition to turbulence in hydrodynamical systems. A large amount of work on this problem has focused on classifying and characterizing the various convection states according to their spatial and temporal behavior. Aside from linear stability analysis of the conductive basic state, theoretical investigations estimate the influence of the nonlinear terms of the governing equations applying suitable perturbations. Busse and co-workers determined the domain where parallel convection rolls are stable (Busse balloon [1,2]). For a comprehensive overview of experimental and theoretical investigations, see [3].

Our objective is to describe the nonlinear dynamics in a finite cylindrical domain, exploring the formation of different patterns as straight rolls, targets, and spirals. We study their stability and look for bifurcations. The occurrence of a variety of convective patterns in a cylinder, partly coexisting simultaneously for equal values of the control parameters, was observed in various experiments and is described in Refs. [4–14]. Theoretical investigations on the generation and stability of those patterns are based mainly on amplitude and phase equations [3,15–17]. In this paper, we study convection and pattern formation in a cylinder by means of the three-dimensional Boussinesq equations applying physical boundary conditions. Since the experiments referred to above differ slightly, as, e.g., in their aspect ratio and Prandtl number, and the described scenarios depended very sensitively on the special experimental setup, as, e.g., the application of sidewall heating, only parts of our results can be compared with the observed pattern dynamics.

Fixing both the aspect ratio and the Prandtl number, the Rayleigh number will be our control parameter. In correspondence with all experiments we found straight and bent rolls with sidewall defects as the only stable pattern near the convective threshold. But for a certain range of the Rayleigh number also targets and spirals appear as coexisting solutions that are stable and robust against finite perturbations, a phenomenon that was observed only in some of the experiments [5]. In other experiments only a sidewall heating causes the generation of targets that evolve to a nonaxisymmetric flow immediately after the switch off [4].

For the cylindrical situation, Buell and Catton [18] and Marqués *et al.* [19] estimated the critical Rayleigh number as a function of the aspect ratio and characterized its dependence on the wave number. With increasing aspect ratio the critical value approaches the limit value of 1708 for all azimuthal wave numbers, which is the critical Rayleigh number for an unbounded layer. Marqués *et al.* showed that for an aspect ratio larger than three, the critical curves of the azimuthal modes come close together and it is thus hard to distinguish which mode is responsible for the instability. In other words, for values slightly above the critical Rayleigh number a variety of modes is unstable simultaneously, and the formation of the resulting pattern requires additional investigations. In this paper, we address the question of which attractors determine the spatial structure of the convective dynamics for moderate Rayleigh numbers. Our aim is to get an understanding of the stability of various solution types as attractors of the full nonlinear problem.

II. BASIC EQUATIONS AND NUMERICS

We are concerned with buoyancy-driven convection in a plane circular fluid layer of thickness d and radius L heated from below. The Boussinesq equations that describe the evolution of the velocity field $\mathbf{v}(r,\phi,z)$ and the deviation $\Theta(r,\phi,z)$ of the temperature from the conductive profile can be written in dimensionless form as

$$P^{-1}\left[\frac{\partial \mathbf{v}}{\partial t}+(\mathbf{v}\cdot\boldsymbol{\nabla})\mathbf{v}\right]=\boldsymbol{\nabla}^2\mathbf{v}-\boldsymbol{\nabla}p+R\Theta\,\mathbf{e_z}, \tag{1}$$

$$\frac{\partial \Theta}{\partial t}+(\mathbf{v}\cdot\boldsymbol{\nabla})\Theta=\boldsymbol{\nabla}^2\Theta+v_z, \tag{2}$$

$$\boldsymbol{\nabla}\cdot\mathbf{v}=0. \tag{3}$$

Here the units of length and time are d and $\tau_T=d^2/\kappa$, repectively, with κ being the thermal diffusivity. The dimensionless parameters are the aspect ratio $a=L/d$, the Prandtl number P, and the Rayleigh number R, defined by

$$P=\frac{\nu}{\kappa}, \quad R=\frac{\alpha g d^3}{\nu\kappa}\delta T, \tag{4}$$

respectively, where ν is the kinematic viscosity, α is the thermal expansion coefficient, g is the gravitational acceleration, and δT is the driving temperature difference. The Rayleigh number R measures the strength of the buoyancy forces and serves as the bifurcation parameter in our calculations.

In correspondence with experiments without external sidewall forcing we assume an insulating jacket with isothermal top and bottom plates on the cylinder as the boundary conditions for the temperature deviation

$$\partial_r \Theta = 0 \quad \text{on} \quad r = a, \quad \Theta = 0 \quad \text{on} \quad z = -\frac{1}{2}, \frac{1}{2}, \quad (5)$$

and no-slip boundary conditions for the velocity field,

$$v_r = v_\phi = v_z = 0 \quad \text{on} \quad r = a \quad \text{and} \quad z = -\frac{1}{2}, \frac{1}{2}. \quad (6)$$

Because of the incompressibility of the velocity field given by Eq. (3), the velocity field is usually expressed by poloidal and toroidal potentials, an appropriate technique in plane and spherical geometries. But for the cylindrical situation the potentials couple at the boundaries and produce numerical instabilities. Thus, we follow Marqués [20] and choose a decomposition that splits the velocity field into its axisymmetric and nonaxisymmetric parts

$$\mathbf{v} = \mathbf{v}_{\text{ax}} + \mathbf{v}_{\text{nonax}}, \quad (7)$$

where

$$\mathbf{v}_{\text{ax}} = \boldsymbol{\nabla} \times \frac{1}{r} f \mathbf{e}_\phi + v_\phi^{\text{ax}} \mathbf{e}_\phi, \quad (8)$$

$$\mathbf{v}_{\text{nonax}} = \boldsymbol{\nabla} \times (\chi \mathbf{e}_r + \psi \mathbf{e}_z). \quad (9)$$

Here we require the axisymmetric part of $\chi(r,\phi,z)$ and $\psi(r,\phi,z)$ to vanish and $f(r,z)$ and $v_\phi^{\text{ax}}(r,z)$ to be independent of ϕ.

The equations for the four potential functions are derived by using the equation of motion but they are not given here. In order to get the equations for the axisymmetric parts f and v_ϕ^{ax}, we multiply Eq. (1) by $\mathbf{e}_\phi$ and $\mathbf{e}_\phi \cdot \boldsymbol{\nabla} \times$, respectively, and multiply Eq. (1) by $\mathbf{e}_r \cdot \boldsymbol{\nabla} \times$ and $\mathbf{e}_z \cdot \boldsymbol{\nabla} \times$ to get the equations for the nonaxisymmetric parts χ and ψ, respectively.

The four potential functions and the temperature deviation Θ are then decomposed into Fourier functions in the azimuthal direction and Chebychev polynomials in the r and z direction. As an example, we set

$$\Theta(r,\phi,z) = \sum_{\substack{j=-N_\phi/2}}^{N_\phi/2-1} \sum_{\substack{l=0 \\ j+l \text{ even}}}^{N_r} \sum_{k=0}^{N_z} \Theta_{jlk} T_l(r/a) e^{ij\phi} T_k(2z). \quad (10)$$

The restriction to even sums $j+l$ is a consequence of the parity at the origin. For instance, a scalar field $\Theta(r,\phi)$ in polar coordinates obeys the condition of even parity $\Theta(-r,\phi) = \Theta(r,\phi+\pi)$. In cylindrical coordinates the vector component v_z shares the same parity, whereas v_r and v_ϕ are odd. The parity of the velocity potentials follows from Eqs. (8) and (9), respectively. According to the even or odd parity of the potential, even or odd sums $j+l$ are included in the decomposition only.

In order to avoid numerical instabilities due to strong negative eigenvalues, we treat the linear terms of the equations with the implicit Euler method. The nonlinear terms are calculated pseudospectrally in the physical space and included explicitly in the time step using second-order Adams-Bashforth integration. This method was already successfully applied and proven to be accurate and efficient in simulations of the Navier-Stokes equations by Tilgner and Busse [21]. To prevent aliasing effects in the fast Fourier transformation we implemented the 2/3 rule in the Fourier decomposed azimuthal direction. We used a resolution of 9 grid points in the vertical direction, 32 points in the azimuthal direction, and 33 points in the radial direction. The time step amounted to 10^{-2} in most of the calculations.

III. NUMERICAL RESULTS

In our numerical investigations we set the Prandtl number $P=1$. With increasing aspect ratio the need of computer memory and processor time increases strongly and, therefore, we fixed the aspect ratio $a=4$ in all of the following calculations. Thus, the results can be compared to the experiments with moderate aspect ratios, as, e.g., described in Ref. [5].

We calculated the eigenvalues of the linear operator depending on the azimuthal wave number and estimated the onset of convection for Rayleigh numbers between 1736 and 1748. This agrees with the results of Marqués et al. [19] (see Fig. 1 therein). From there, one can roughly estimate the critical Rayleigh numbers of the modes $j=0,\ldots,4$ to be about 1750 for our situation of an aspect ratio equal to 4. Since the primary instability occurs in a narrow band of Rayleigh numbers for all small azimuthal wave numbers, we expect the appearance of different coexisting solution branches.

In the following we measure the Rayleigh number in terms of $\epsilon = R/R_c - 1$, where R_c is the critical Rayleigh number of 1736. As initial patterns we used random distributions to the mode coefficients as well as targets and spirals and performed simulations for several horizontal diffusion times $\tau_h = a^2 \tau_T$ to reach the attractors.

For small ϵ above the onset of convection the resulting attractor is a time-independent defect-free state consisting of seven straight rolls along the diameter [Fig. 1(a)]. Following this solution branch by increasing the bifurcation parameter ϵ the rolls bend as to end perpendicular to the boundary, a state in which two wall foci are generated [Fig. 1(b)]. This phenomenon was observed in several experiments and results from boundary effects [3]. A summary of all solution branches, their interval of stability and their symmetry, is given in Table I. The pattern consisting of seven straight rolls [Fig. 1(a)] and the following pattern for increased values of the Rayleigh number consisting of seven bent rolls with two foci [Fig. 1(b)] seem to belong to the same branch and are not distinguished here. They are denoted as seven straight/bent rolls in Table I. Before we proceed, the symmetry notation will be explained. Due to the cylindrical geometry, the Boussinesq equations are invariant with respect to the $\mathbf{O}(2) \times \mathbf{Z}_2$ symmetry, where the $\mathbf{Z}_2$ group accounts for the reflection in the midplane [22]. This reflection will be denoted by γ. In the convection state the original symmetry
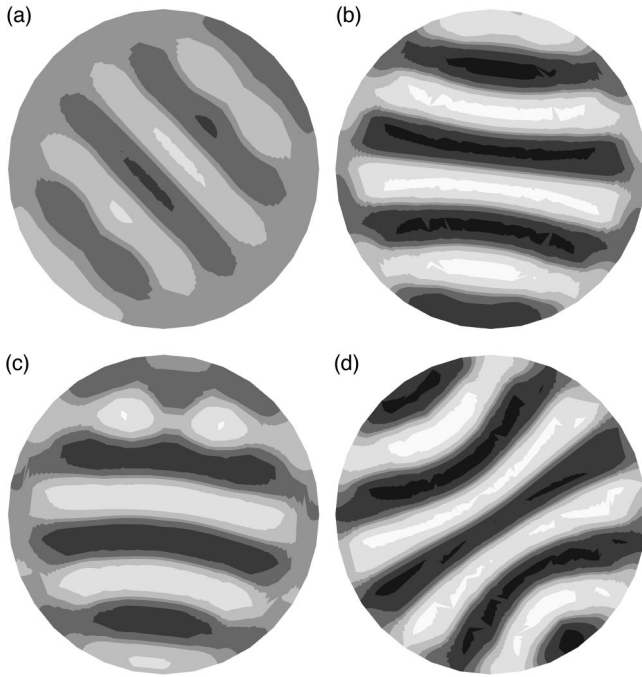
FIG. 1. Temperature deviation Θ in the cross section $z=0$. Dark colors denote negative Θ (corresponding to a cold descending fluid), bright colors denote positive Θ (warm ascending fluid). (a) $\epsilon=0.04$ (seven straight rolls), (b) $\epsilon=0.38$ (seven bent rolls forming two wall foci), (c) $\epsilon=0.21$ (seven rolls with one wall focus), (d) $\epsilon=0.73$ (eight rolls with two wall foci).

is broken, and the resulting subsymmetry of the different branches can be generated by three discrete transformations. In the plots of Fig. 1, these are the midplane reflection γ, a reflection κ that acts as a reflection in the axis through the midpoint perpendicular to the rolls, and a rotation by π about the midpoint denoted by R_π. We determined the symmetry of different solution branches by studying corresponding transformations of the Fourier coefficients. For example, the symmetry of the first branch, the pattern of seven straight/bent rolls, is given by the reflection κ, the midplane reflection combined with the rotation, $\gamma \cdot R_\pi$, and the combination of both transformations $\kappa \cdot \gamma \cdot R_\pi$.

Coexisting with this primary branch we found patterns of seven rolls with only one wall focus [Fig. 1(c)] and a branch with eight rolls [Fig. 1(d)]. The patterns of seven rolls in Fig. 1(c) are bent in one preferred direction and thus create only one wall focus visible on the bottom of the figure. The two bloblike structures at the upper side of the figure are no foci and correspond to local deformations of the rolls. From Fig.

TABLE I. Overview of the solution branches. Values of the intervals are determined with tolerances of 0.03.

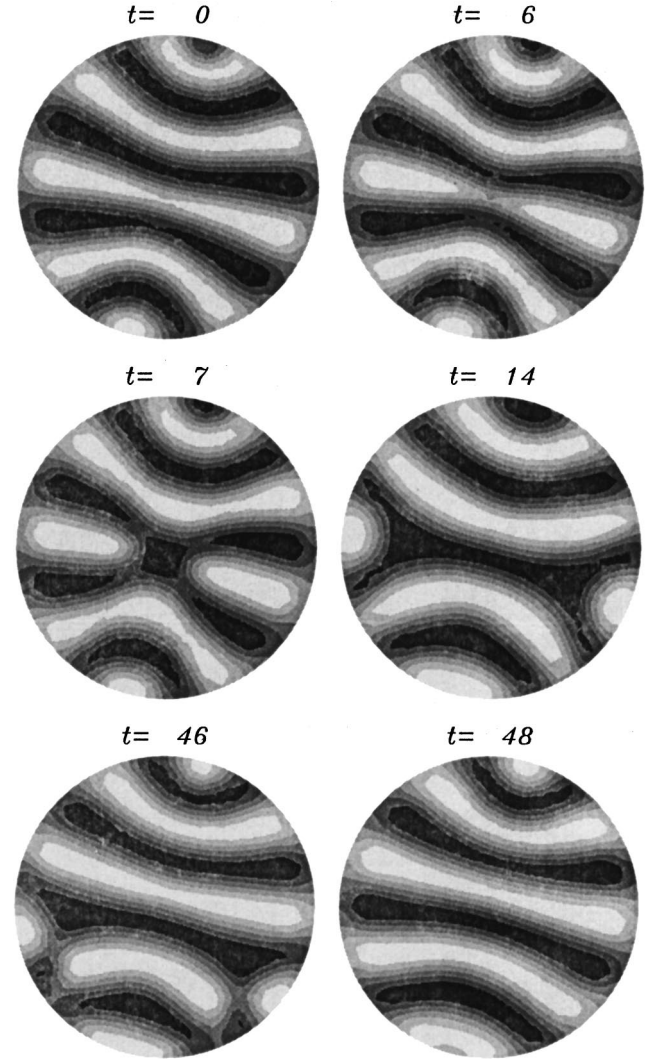| Branch	Stability range for ϵ	Symmetries
7 straight/bent rolls	$0, \ldots, 0.41$	$\kappa, \gamma \cdot R_\pi, \kappa \cdot \gamma \cdot R_\pi$
7 bent rolls with one wall focus	$0.12, \ldots, 0.24$	κ
8 bent rolls with two wall foci	$0.24, \ldots, 0.82$	$\kappa, R_\pi, \kappa \cdot R_\pi$
3-targets	$0.3, \ldots, 1.04$	$\mathbf{O}(2)$
spirals	$0.14, \ldots, 0.35$	rot. wave sym.

FIG. 2. The skew-varicose instability generates a cycle of climbing and gliding defects. Snapshots of the cycle are shown for $\epsilon=0.9$, time is given in τ_T.

17 in [10] we found evidence that these patterns can be observed in experiments but they were not explicitly mentioned there.

The solution branch of eight bent rolls, Fig. 1(d) shows this pattern for $\epsilon=0.73$, is stable over a larger range of Rayleigh numbers, and we could trace it up to $\epsilon \approx 0.8$. It loses its stability due to the skew-varicose instability [17], and a cycle of defect dynamics is initiated. The skew-varicose instability causes one roll to break off, generating two defects. The defects climb to the boundary, merge with neighboring rolls and, eventually, the original defect-free pattern is recovered. Afterward the cycle starts again by compression of inner rolls. The whole cycle is presented in Fig. 2. The effect of climbing and gliding of defects generated by pinching of rolls was observed in experiments [7] that were performed with comparable parameter values. The qualitative agreement of the whole scenario is striking, especially the defect cycle shown in Fig. 2, with the defect dynamics presented in Ref. [7]. To determine the temporal behavior of solutions, we examined the coefficients in the polynomial expansions of the potentials and of the temperature deviation as, e.g., the Θ_{jlk} defined in Eq. (10). Here the cycle of dislocation nucle-

ation and roll pinching corresponds to a complicated but periodic trajectory. This contrasts with experiments where the defect cycle appears chaotically [7]. In our simulations with an aspect ratio of $a=4$ no chaotic trajectories were found. The cycle seems to be very sensitive to changes in the Rayleigh number and the used numerical resolution. Thus, we checked the results partly with higher resolution of 64 grid points in the azimuthal direction but no chaos was found for $a=4$. We observed that up to $\epsilon=2.8$ either the periodic behavior is conserved or the pattern relaxes to a stationary pattern with three wall foci.

A different picture emerges for a larger aspect ratio. Matching to the experiments of Pocheau *et al.* [7] we performed simulations for an aspect ratio of $a=7.66$. Because of the high numerical resolution that is required for this larger aspect ratio we could perform only simulations over a shorter time period. We obtained evidence that the defects appear chaotically. The pinching of the rolls is driven by a cyclic generation of new rolls from the two wall foci.

Starting simulations with random initial conditions, one of the branches described above is the attractor that is reached in the time asymptotic limit. In order to look for target and spiral patterns, we prepared initial conditions in which relevant modes of these patterns are prescribed. For ϵ slightly above the onset we found both targets and spirals to be unstable. After transition times of about four horizontal diffusion times τ_h the final attractor is a state consisting of straight or bent rolls.

We observed stable target solutions with three rolls per radius (three-target) in the range of $\epsilon=0.3,\ldots,1$. In this range the target pattern survives for more than $10\tau_h$ and seems to be an attractor. In order to check the stability of the targets, all modes, including the non-axisymmetric modes, were perturbed by adding random numbers to the mode coefficients with a value proportional to the inverse of the wave number ($\sim 1/|k|$). Up to an amplitude of about $\pm 30\%$ of the largest modes, the perturbed initial state converged to the original target solution.

For ϵ larger than 1.04 we found an instability in which the center of the target moves toward the boundary, breaking the axisymmetry (Fig. 3, upper right). This instability is called focus instability and has been investigated in a number of experiments for moderate and large aspect ratios [5,10,23] and in theoretical approaches [17]. In the experiments the final pattern constitutes a steady state and is called off-center target. In our simulations with an aspect $a=4$ the off-center target is not stable and the outer roll breaks up at the boundary, producing a state of straight rolls. Snapshots of this transition are shown in Fig. 3. The reason for this distinction is presumably a consequence of the smaller aspect ratio we used. In order to prove this conjecture we performed some simulations with an aspect ratio of $a=8$ that corresponds to the experiments in Ref. [5]. The off-center targets appeared to be stable for a large range of Rayleigh numbers.

For ϵ smaller than 0.3 the three-target loses stability to a target with four rolls per radius by generating an additional roll in the center. The four-target is a transient pattern that is in turn subject to the focus instability.

We estimated the wave numbers of target patterns and solutions consisting of bent rolls. For each target pattern we measured the distance between the two rolls near the center.
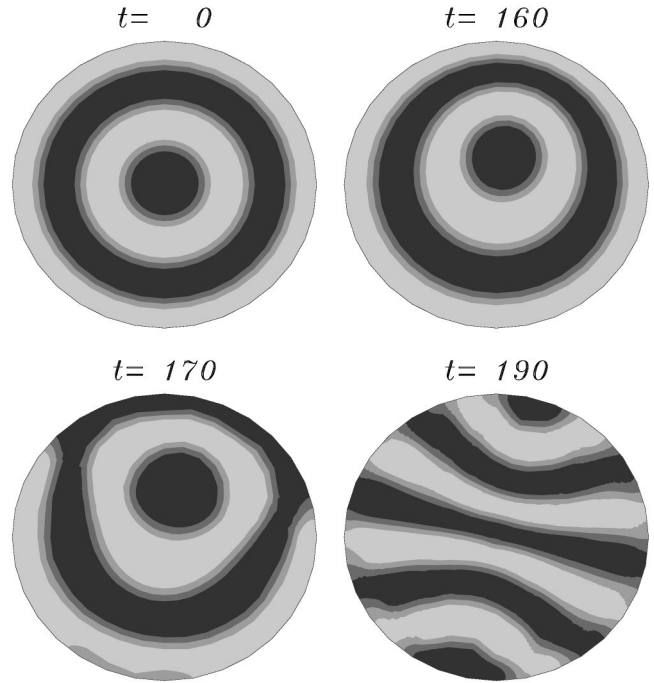

FIG. 3. Snapshots of the transition from the target state to a pattern of bent rolls for $\epsilon=1.07$. Time is given in τ_T.

The resulting wave numbers are inside the Busse balloon (Fig. 4, diamond symbols). The distance of the inner rolls adjusts for small ϵ reducing the outer roll but remains relatively constant for larger ϵ until the solution is subject to the focus instability. We applied a Fourier decomposition to the patterns of bent rolls and determined the average wave number (squares in Fig. 4). The plot reveals that the onset of time dependence produced by the generation of the defect cycle coincides with the intersection of the skew-varicose line in the Busse balloon.

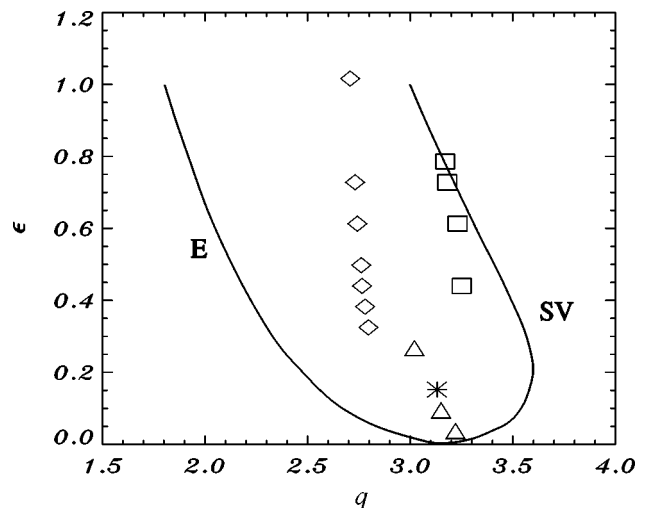One-armed spirals are stable from $\epsilon=0.14,\ldots,0.35$.

FIG. 4. ϵ vs wave number of the pattern for stable three-targets ($\diamond$) and bent rolls solutions ($\triangle$, seven rolls; *, seven rolls with one focus; $\square$, eight rolls). Both solution types possess wave numbers inside the Busse balloon which is given by the Eckhaus (E) and skew-varicose (SV) instability line (Busse balloon courtesy of W. Pesch).
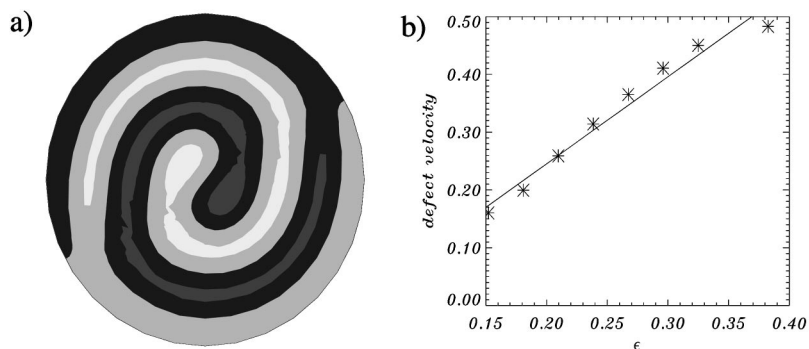
a)

b)

FIG. 5. (a) Stable spiral solution at $\epsilon = 0.27$. (b) Velocity of the spiral defect vs ϵ, the straight line is the result of a least-square fit.

Above this range they are unstable to patterns of bent rolls. An example of a spiral that we simulated over $30\tau_h$ is given in Fig. 5(a). We see that the spiral has ''knots'' in the radial direction yielding a nonhomogeneous amplitude distribution in the radial direction. The spiral shown in Fig. 5(a) rotates uniformly in a counterclockwise direction. Spiral rotation can be understood as the motion of the outer defect. In our simulations the defect is the point where the spiral touches the boundary. We can thus compare our results to the measurements of defect motion in spirals published by Plapp *et al.* [24]. The authors find experimentally a linear dependence of the velocity of the outer defect on ϵ. Our calculations show linear dependence [Fig. 5(b)] though the defect motion is faster than expected from extrapolation from the experiments.

IV. CONCLUSION

In conclusion, we found stable target patterns and rotating spirals for the relatively small aspect ratio $a = 4$ if $\epsilon > 0.3$ and $\epsilon > 0.15$, respectively. We determined the lower and upper stability limits of targets and spirals as well as the transition for critical ϵ. For smaller ϵ both solution types are unstable

to patterns of bent rolls. The upper stability boundary of targets is given by the focus instability, though the resulting off-center pattern is unstable to patterns of straight/bent rolls. First simulations with an aspect ratio of $a = 8$ have shown a stable off-center target.

We could confirm the cycle of climbing and gliding of defects for the pattern of straight rolls. Chaos was found for a larger aspect ratio of about $a = 8$, whereas smaller aspect ratios yield strictly periodic cycles. Calculations of the wave number of the time-independent patterns have shown that the skew-varicose boundary is responsible for the instability even for relatively small aspect ratios.

[1] F. H. Busse, in *Hydrodynamic Instabilities and the Transition to Turbulence*, edited by H. L. Swinney and J. P. Gollub, Topics in Applied Physics, Vol. 45 (Springer-Verlag, Berlin, 1985), pp. 97–133.

[2] F. Busse, in *Mantle Convection, Plate Tectonics and Global Dynamics*, edited by W. R. Peltier (Gordon and Breach, New York, 1989), pp. 23–95.

[3] M. Cross and P. Hohenberg, Rev. Mod. Phys. **65**, 851 (1993).

[4] V. Croquette, M. Mory, and F. Schossler, J. Phys. (France) **44**, 293 (1983).

[5] V. Steinberg, G. Ahlers, and D. S. Cannell, Phys. Scr. **32**, 534 (1985).

[6] G. Ahlers, D. Cannell, and V. Steinberg, Phys. Rev. Lett. **54**, 1373 (1985).

[7] A. Pocheau, V. Croquette, and P. L. Gal, Phys. Rev. Lett. **55**, 1094 (1985).

[8] M. Heutmaker, P. Fraenkel, and J. Gollub, Phys. Rev. Lett. **54**, 1369 (1985).

[9] M. Heutmaker and J. Gollub, Phys. Rev. A **35**, 242 (1987).

[10] V. Croquette, Contemp. Phys. **30**, 153 (1985).

[11] Y. Hu, R. E. Ecke, and G. Ahlers, Phys. Rev. E **48**, 4399 (1993).

[12] M. Assenheimer and V. Steinberg, Nature (London) **67**, 345

(1994).

[13] E. Bodenschatz, W. Pesch, and G. Ahlers, Annu. Rev. Fluid Mech. **32**, 709 (2000).

[14] V. Getling, *Rayleigh-Bénard Convection, Structures, and Dynamics*, of Advanced Series in Nonlinear Dynamics Vol. 11 (World Scientific, Singapore, 1995).

[15] Y. Pomeau and P. Manneville, J. Phys. (France) Lett. **40**, 609 (1979).

[16] J. C. Buell and I. Catton, Phys. Fluids **29**, 23 (1986).

[17] A. C. Newell, T. Passot, and M. Souli, J. Fluid Mech. **220**, 187 (1990).

[18] J. C. Buell and I. Catton, J. Heat Transfer **14**, 255 (1983).

[19] F. Marqués, M. Net, J. Massaguer, and I. Mercader, Comput. Methods Appl. Mech. Eng. **110**, 157 (1993).

[20] F. Marqués, Phys. Fluids A **2**, 729 (1990).

[21] A. Tilgner and F. Busse, J. Fluid Mech. **332**, 1 (1997).

[22] M. Golubitsky, I. Stewart, and D. G. Schaeffer, *Singularities and Groups in Bifurcation Theory, Vol. II* (Springer, New York, 1988).

[23] Y. Hu, R. E. Ecke, and G. Ahlers, Phys. Rev. Lett. **72**, 2191 (1994).

[24] B. Plapp, D. Egolf, E. Bodenschatz, and W. Pesch, Phys. Rev. Lett. **81**, 5334 (1998).